

See discussions, stats, and author profiles for this publication at: <https://www.researchgate.net/publication/5337917>

Uniform Threshold Intensity Distribution-Based Quantitative Multivariate Imaging Cytometry

ARTICLE *in* ANALYTICAL CHEMISTRY · AUGUST 2008

Impact Factor: 5.64 · DOI: 10.1021/ac800452x · Source: PubMed

CITATIONS

12

READS

20

3 AUTHORS, INCLUDING:



Pravin Naoghare

National Environmental Engineering Resea...

27 PUBLICATIONS 147 CITATIONS

SEE PROFILE



Joon Myong Song

Seoul National University

107 PUBLICATIONS 2,409 CITATIONS

SEE PROFILE

Uniform Threshold Intensity Distribution-Based Quantitative Multivariate Imaging Cytometry

Pravin K. Naoghare, Min Jung Kim, and Joon Myong Song*

Research Institute of Pharmaceutical Sciences and College of Pharmacy, Seoul National University, Seoul 151-742, South Korea

Implementation of quantitative analytical approaches to image-based cellular assays remains a major challenge. We disclose a tool to achieve automatic rapid quantitative cellular imaging analysis based on uniform threshold intensity distribution. An acousto-optic tunable filter-based, quantitative multivariate imaging cytometer was set up to elucidate drug-induced cell death dynamics via cell viability and apoptosis/necrosis measurements in the human myeloid leukemia cell line, HL-60. Cells were treated with various drugs (camptothecin, naringenin, sodium salicylate) at different concentrations and time intervals. The developed protocol can directly depict and quantitate targeted cellular moieties, subsequently enabling a method that is applicable to various cellular assays with special reference to next generation drug discovery screening. This may also complement certain flow-cytometric measurements in studying quantitative physiology of cellular systems.

Cell-based assays offer an invaluable tool in basic research applications and drug screening techniques for the analysis of vague intra- and extracellular matrix interactions to better understand cellular responses. These assays explore various applications to validate previously unknown targets, monitor cellular events, and screen compounds for efficacy and biosafety. Cellular assays are now used extensively to ascertain drug-mediated toxicity and cellular responses and to discover new chemical entities in the early phase of drug discovery using in vivo and in vitro models.¹ Recently, rapid in vitro screening methods were utilized for intense drug discovery to predict in vivo drug response^{2,3} and to minimize the use of animal-based experiments. However, in vitro assays often trigger many complex drug-induced cellular pathways that cannot be predicted using biochemical assays.⁴ For example, caspase activation⁵ epidermal growth factor receptor (ErbB3) activation⁶ phosphatidylserine (PS) externalization,⁷ etc., are the most complex phenomena of the cell cycle pathway. These

complexities have contributed to increased use of cell-based screening assays to predict the drug-induced cellular response,^{8,9} through cell viability, cytotoxicity, apoptosis/necrosis measurements, and many other parameters. Most of the available techniques used for cellular assays are based on either imaging or spectroscopic analysis. However, each of these techniques has its own advantages and disadvantages. Combined use of broadband excitation sources and glass filters possessing a certain transmission wavelength range inevitably causes a practical limitation in high-resolution discrimination of individual fluorophores with broad emission spectra.^{10–12} Other conventional spectroscopic techniques, being point measurement methods, do not offer simultaneous discrimination of cell death pathways. Typically, they provide signal detection at every wavelength within a spectral range, but only for a single analyte spot.¹³ Flow cytometry, which is now routinely preferred as a rapid tool for cellular assays, records the signal detected for each event at different detectors. But the discrimination of an individual fluorophore is based on fluorescence detectors with a predetermined range ($\sim\pm 30$ nm) for wavelength discrimination, and therefore, the individual fluorophore cannot be discerned at a single wavelength. These features can lead to poor spectral resolution while analyzing multiple fluorophores having broad emission spectra. Imaging-based analysis is another option for understanding cell death dynamics. It can remunerate limitations inherent to flow cytometry by virtue of monitoring an individual live cell over time.¹⁴ For example, cellular aggregation leading to false statistical results in flow cytometry can be observed and corrected by improved cellular assay in the imaging technology. But, traditional imaging tools such as optical microscope are optical filter-based instruments that acquire all photons emitted from a sample to the detector within a specific wavelength range (band-pass). Thus, multicolor/multicomponent imaging analysis can only be possible if images are created with careful choice of a filter

* To whom correspondence should be addressed. E-mail: jmsong@snu.ac.kr. Phone: +82 2 880 7841. Fax: +82 2 871 2238.

- (1) Colombo, P.; Gunnarsson, K.; Iatropoulos, M.; Brughera, M. *Int. J. Oncol.* **2001**, *19*, 1021–1028.
- (2) Bursch, W.; Paffe, S.; Putz, B.; Barthel, G.; Schulte-Hermann, R. *Carcinogenesis* **1990**, *11*, 847–853.
- (3) Kanno, S.-I.; Tomizawa, A.; Ohtake, T.; Koiwai, K.; Ujibe, M.; Ishikawa, M. *Toxicol. Lett.* **2006**, *166*, 131–139.
- (4) Krishna, R.; Mayer, L. D. *Eur. J. Pharm. Sci.* **2000**, *11*, 265–283.
- (5) Bernal, F.; Tyler, A. F.; Korsmeyer, S. J.; Walensky, L. D.; Verdine, G. L. *J. Am. Chem. Soc.* **2007**, *129* (9), 2456–2457.
- (6) Lin, C.-W.; Ting, A. Y. *J. Am. Chem. Soc.* **2006**, *128* (14), 4542–4543.

- (7) Shynkar, V. V.; Klymchenko, A. S.; Kunzelmann, C.; Duportail, G.; Muller, C. D.; Demchenko, A. P.; Freyssinet, J.-M.; Mely, Y. *J. Am. Chem. Soc.* **2007**, *129* (7), 2187–2193.
- (8) King, M. A.; Radicchi-Mastroianni, M. A. *Cytometry* **2002**, *49*, 28–35.
- (9) Kanno, S.; Tomizawa, A.; Ohtake, T.; Koiwai, K.; Ujibe, M.; Ishikawa, M. *Toxicol. Lett.* **2006**, *166*, 131–9.
- (10) Izuishi, K.; Furuse, J.; Kinoshita, T.; Konishi, M.; Tajiri, H. *Heptaogastroenterology* **2003**, *50* (50), 366–7.
- (11) Leonhard, M. *Diagn. Ther. Endosc.* **1999**, *5*, 145–154.
- (12) Ehrhardt, A.; Stepp, H.; Irion, K. M.; Stummer, W.; Zaak, D.; Baumgartner, R.; et al. *Med. Laser Appl.* **2003**, *18*, 27–35.
- (13) Shonat, R. D.; Wachman, E. S.; Niu, W.; Koretsky, A. P.; Farkas, D. L. *Biophys. J.* **1997**, *73* (3), 1223–1231.
- (14) Gordon, A.; Colman-Lerner, A.; Chin, T. E.; Benjamin, K. R.; Yu, R. C.; Brent, R. *Nat. Methods* **2007**, *4* (2), 175.

set and fluorophores to limit the band-pass range and to minimize spectral overlap between detection wavelength regions, respectively.

To date, there is no well-defined protocol for automatic counting of the total number of cells present on an assay platform from an image containing a dense cell population without cellular staining. Automatic quantitative cellular imaging at the bright-field microscopic mode will be an exceptional tool for biologists because it will provide not only a cellular image but also a large amount of statistical information. First, automatic cell viability measurements can be achieved through quantitative cellular imaging. This will have great significance especially to cell culture and bioreactors laboratories that employ cell viability measurements for the maintenance of large cell cultures. This might completely eliminate the need for a hemocytometer, which requires manual cell counting and results in gaining erroneous data during cellular assays, e.g., trypan blue cell viability assay. This may be due to the overestimation of results due to user-to-user variation, increase in time frame, and low statistical confidence as less number of cells are counted. The main obstacles in automatic cell counting from cell images are uneven cellular morphology, high background noise, culture contaminants, and several other impeding factors, e.g., serum protein coagulants, and most importantly, intracellular variation in z values, i.e., the distance between the microscope objective and a cell with respect to the sample platform. In particular, uneven intracellular grayscale intensity distribution in an image can prevent selection of a single cell as a single cell when a parameter such as light contrast is set to choose cells against the background image. This makes it impossible to automatically count cells that satisfy the applied parameter condition. As a result, quantitative imaging analysis at the bright-field microscopic mode has not been a practical tool for biologists. On the other hand, imaging analysis often faces problems due to rapid photobleaching and the narrow excitation spectrum of commercially available fluorophores, which limit the overall utility of imaging systems.¹⁵ In order to elucidate the molecular mechanism involved in triggering targeted biomolecules, real-time monitoring of cellular events is needed. Therefore, the present need is to implement quantitative analytical approaches¹⁶ in image-based cellular assays and to develop a protocol to eliminate the obstacles inherent in the present assay methods. The compatibility of image-based cell counting with various cellular assays is always in question. In this context, implementation of simultaneous monitoring of cellular images as a function of wavelength is a very powerful approach for an automatic image-based cell counting system to permit multivariate profiling for cellular assays.

In this study, we have implemented quantitative analytical approaches in image-based cellular assays based on uniform threshold intensity distribution (TID) through quantitative multivariate imaging (QMI) cytometry. The QMI cytometer is capable of performing wide arrays of automated, quantitative, and multivariate cellular assays via single-cell monitoring over time. Here, we demonstrated its utility through quantitative cell viability and apoptosis/necrosis measurements in the drug-treated human myeloid leukemia cell line, HL-60. An approach employing region selection to slightly defocused, background-nullified and threshold

images facilitated rapid quantitative measurements during cellular assays. This provided uniform TID over the objects (cells), which is necessary for automated quantitative analysis. This multispectral and multicolor imaging also allowed efficient discrimination of simultaneous cellular events (i.e., apoptosis and necrosis) triggered by anticancer drugs by facilitating an entire emission spectrum at an individual wavelength. Moreover, quantum dot (Qdot)-based QMI cytometry allowed photostable detection of cellular events over the tunable wavelengths, making the assay more robust and compatible for live-cell monitoring. The developed protocol offers imaging and quantitative analysis of targeted cellular moieties, which can be further applied to various cellular assays in combination with snapshot methods. With the advent of high-throughput drug screening technology, the hype surrounding virtual screening has passed. But, we still struggle with diagnostic errors that arise from the lead identification tools. In this context, QMI cytometry can pave the way for new generation anticancer drug screening.

MATERIALS AND METHODS

Cell Culture. To characterize the drug-induced cell death pathway in leukemia cells, the HL-60 cell line was obtained from the Korean Cell Line Bank (KCLB, Seoul, Korea) and cultured in RPMI-1640 medium (GIBCO-BRL) supplemented with heat-inactivated FBS (10% v/v), sodium bicarbonate (24 mM), penicillin (60 $\mu\text{g}/\text{mL}$), and streptomycin (100 $\mu\text{g}/\text{mL}$) in 25-cm² cell culture flasks (Nunclon Delta, Intermed). Cells were grown under standard conditions, in a 37 °C humidified incubator containing 5% CO₂ (NuAire).

Drug Treatment. Typically, cells (4.5×10^5 cells/mL) were treated with one of three anticancer drugs, camptothecin (CAM), naringenin (NAR), and sodium salicylate (Na-Sal), all purchased from Sigma (St. Louis, MO). Prior to drug treatment, the cells were cultured overnight so that they were in log-phase growth. Stock solutions of 1 M NAR and 1 mg/mL CAM were prepared in dimethyl sulfoxide (DMSO); Na-Sal (1M) stock was prepared in deionized autoclaved water. Immediately before the experiment, 20 μL of CAM stock solution was added to 2 mL of phosphate-buffered saline (PBS) to yield a 28.7 μM working solution. Cells were treated with various concentrations of drugs, i.e., CAM (150 and 287 nM), NAR (0.5 mM), and Na-Sal (2.5–10 mM) for 12, 6, and 12 h, respectively. For better statistical understanding, three independent experiments were performed for each particular drug concentration/time interval. The final concentration of DMSO in the medium was carefully kept below 0.5% to nullify its toxicity. Cells not exposed to drugs, but supplemented with the same concentration of DMSO, and grown under the same condition as drug-treated cells, were used as controls.

Staining. (a) *Cell Viability Assay.* Cells (1×10^5) were counted using a hemocytometer and treated with one of three anticancer drugs. After drug treatment, cells were washed twice, resuspended in 100 μL of 10 mM PBS, and incubated with 10 μL of propidium iodide (PI; BD Biosciences) for 15 min at room temperature in the dark. The cell suspension was centrifuged, and the pellet was dissolved in 10 μL of PBS and subjected to QMI cytometry. For trypan blue (Biological Industries, Beth Haemek, Israel) assays, cells were resuspended in trypan blue solution (0.25% in PBS) and incubated at room temperature for 5 min. Excess trypan blue

(15) Stephens, D. J.; Allan, V. J. *Science* **2003**, 300; www.sciencemag.org.

(16) Loo, L-H.; Wu, L. F.; Altschuler, S. J. *Nat. Methods* **2007**, 4 (5), 445.

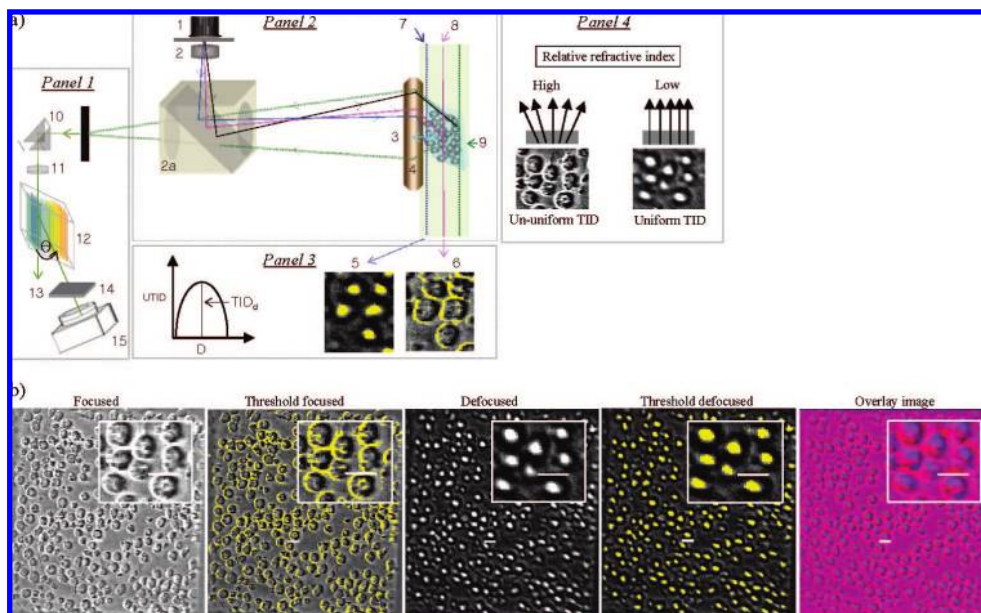


Figure 1. (a) Schematic of the QMI system. Panel 1 shows cells in focal and defocal planes. Panel 2 shows AOTF alignment. Panel 3 refers to confocal micrographs of defocused and focused images. Graphical representation of uniformity of threshold intensity distribution (UTID) versus D (distance away from the focal point) showed TID_d at $20\ \mu\text{m} \pm 2$. Here, 1. Laser, 2. Exciter, 2a. Beam splitter, 3. Z value, 4. Objective lens ($60\times$), 5. Defocused threshold image, 6. Focused threshold image, 7. Defocal plane, 8. Focal plane, 9. Sample, 10. Prism, 11. Focusing lens, 12. AOTF, 13. Undiffracted beam, 14. Diffracted beam, 15. Detector, θ . Bragg angle (the angle between diffracted and undiffracted beam). Panel 4 shows difference of phase contrast of cells in focal (ununiform TID) and defocal plane (uniform TID). (b) Developed methodology for quantitative analysis. For each image, a magnified view of selected cells is shown in an inset. Focused, threshold focused, defocused, threshold defocused, and overlay image depicts ~ 180 cells.

was removed by washing the cells twice with PBS. Percent cell viability after the drug treatment was determined using QMI cytometry.

(b) Apoptosis and Necrosis Assay. After drug treatment, cells (1×10^5) were washed twice and resuspended in $100\ \mu\text{L}$ of calcium-enriched binding buffer (BD Biosciences) to enable Annexin V binding to PS. The cell suspension was incubated at room temperature for 15 min in the dark with $5\ \mu\text{L}$ of Annexin V-Biotin (BD Biosciences). Cells were washed again to remove any unbound Annexin V-Biotin from the cell suspension and resuspended in $100\ \mu\text{L}$ of binding buffer. This was followed by incubation with $10\ \text{nM}$ Qdot–streptavidin conjugate (Q10141MP, Invitrogen) and $10\ \mu\text{L}$ of PI for 15 min at room temperature in the dark. Finally, the cell suspension was centrifuged, and the pellet was dissolved in $10\ \mu\text{L}$ of binding buffer and subjected to QMI cytometry. Sometimes, aggregation of Qdots can produce misleading results due to improper binding with the target biomolecule.¹⁹ It is also possible that PS moieties on the cell membrane are not well recognized due to self-aggregation of Qdots around Annexin V molecules. Therefore, to avoid possible aggregation issues, the Qdots were dissolved in binding buffer and vortexed before the staining procedure. After treatment with the Qdots and PI, drug-induced cellular responses were monitored using the constructed QMI cytometer.

Construction of QMI System. As shown in Figure 1 (panel 1). A 488-nm beam from an Ar ion laser (Melles Griot Laser Group, Carlsbad, CA) was used to excite the drug-treated cells in a cell culture plate mounted on the sample stage. The laser beam, which was purified by an interference filter (U-MGFPHQ, Olympus, Tokyo, Japan), was reflected by a dichromatic mirror and focused onto the treated cells with a $60\times$ microscope objective lens

(Olympus). Fluorescence emission from apoptotic or necrotic cells was collected by the same microscope objective lens, passed through a dichromatic mirror, and directed at a right angle by a prism. A lens positioned in front of the acousto-optic tunable filter (AOTF; TEAF10-0.45-0.7-S, Brimrose) was used to reduce the fluorescence beam diameter so that the entire fluorescence beam passed through the $10 \times 10\ \text{mm}$ AOTF window. The AOTF permitted transmission of the diffracted beam with desired Bragg angle (θ) at a particular wavelength through the use of a birefringent crystal (panel 2). Thus, the diffracted beam wavelength could be scanned rapidly. The fluorescence beam transmitted from the AOTF was then detected by a charge-coupled device (CCD) camera. A long-pass filter was located in front of the CCD camera to remove the laser scattering. The detection limit of fluorescein emission was found to be $1 \times 10^{-8}\ \text{M}$ with the constructed QMI system.

Data Acquisition and Quantitative Analysis. The exposure time of the CCD camera was adjusted to 1 s. The fluorescence image at a particular wavelength was obtained by the CCD camera as a function of AOTF frequency sweeping. The AOTF was scanned in the spectral region from 463 to 688 nm with a 3.75-nm interval and a scanning rate of 1 wavelength/s (maximum scanning rate of AOTF, 1 Hz). The spectral resolution of the AOTF is adjustable up to 0.1 nm. The AOTF frequency sweeping and the CCD image acquisition were operated coincidentally so that a total of 60 frames of individual CCD images corresponded to the fluorescence emission at the individual wavelengths scanned by the AOTF. The entire scanning process was completed in 60 s. A new strategy was applied to facilitate rapid, quantitative, imaged-based analysis irrespective of cellular morphology. Focused, slightly defocused, stack and background (without sample) images

were captured for each sample at an identical xy -axis position of the sample platform. This was followed by applying background correction and threshold intensity to a defocused image. The schematic of this approach is given in Figure 1 (panel 3), wherein cell images are depicted in defocal and focal planes. Focused image (focal plane) does not allow uniform TID over the objects (cells) due to the intercellular variation in Z value. In contrast, a slightly defocused ($20\ \mu\text{m} \pm 2$ away from the focal point) image (defocal plane) allowed uniform TID over the entire object and facilitates automated region selection, i.e., one region per object. Image analysis was carried out using commercially available software, MetaMorph, Version 7.1.3.0 (Molecular Devices). Unwanted contaminants (e.g., serum protein coagulants, cell debris, etc.) were removed by selective width selection using object selection parameters. The filter range was adjusted to $1.84211 < N < 10$ (where N is the number of objects) by considering the average width of an HL-60 cell to be $10\ \mu\text{m}$. Image masks were generated by omitting contaminants. Each object in the mask image was automatically marked as an individual object by creating the region around the object. All the regions were then saved and loaded on individual image frames of the stack file to allow automatic region measurements (optical density, average gray value, Z position, angle, distance, area, width, image plane, elapsed time, stage label, wavelength, region label, intensity S/N, threshold area, etc.) of all the objects along the AOTF sweeping wavelengths (463–688 nm). Approximately 300 cells were analyzed. Finally, all the data were automatically exported to a spreadsheet in Microsoft Excel to allow graphical and quantitative data representation. The average fluorescence intensities of all the selected regions were taken at 523 and 617 nm to estimate the total number of Qdot (apoptotic) and PI (necrotic/dead)-stained cells, respectively. Relative fluorescence intensity values based on control samples were fixed in each cellular assay to differentiate stained versus unstained cells.

RESULTS

Effect of Defocusing on Threshold Intensity Distribution.

TID is a critical aspect in assigning an individual region around a cell. Uneven TID may lead to assignment of two or more regions to an individual cell. Figure 1b shows focused, threshold focused, defocused, threshold defocused, and overlapped images, depicting ~ 180 cells. Obtained data suggest that TID was uneven in a tightly focused image. Interestingly, a uniform TID can be observed in the threshold defocused image. It can be seen that almost all the cells were assigned with uniform and consolidated intensities that further resulted in assignment of a single region around an individual cell and, thus, subsequently led to accurate quantitative measurements. To better understand the effect of defocusing on image thresholding, three representative cells were taken and analyzed for TID (Figure 2). As seen in Figure 2, the distribution of grayscale values (indicated by different colors) in defocused and focused images were different. In the focused image, the average grayscale values were similar in certain patches of the cell, whereas the defocused image showed similarities in grayscale values in the intracellular regions. Thus, more than one region was assigned to a tightly focused cell after thresholding the image. However, slight defocusing of the image away from the focal plane (threshold defocused image) led to a uniform TID. The same can

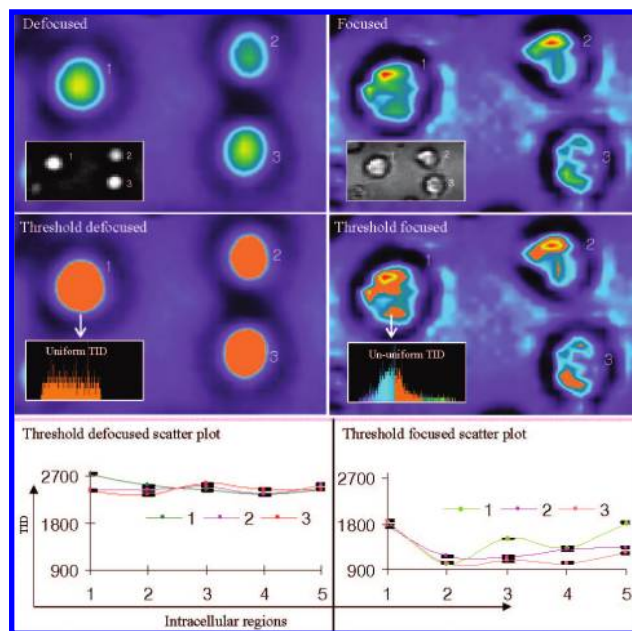


Figure 2. Effect of image defocusing on TID. For better understanding, three representative cells (1, 2, 3) were taken for analysis. Focused, focused threshold, defocused, defocused threshold, and a scatter graphs (indicating intracellular grayscale values of 3 representative cells) can be seen. Insets in focused and defocused image shows grayscale images of three representative focused and defocused cells. Inset in threshold focused and threshold defocused image shows histogram obtained from cell 1 of the respective image depicting an ununiform and uniform TID, respectively.

also been seen in Figure 1, panel 3. The uniformity of TID tended to decrease before and after the distance (d) away from the focal plane. Maximum uniform TID (TID_d) was observed at $20 \pm 2\ \mu\text{m}$ away from the focal point. To understand the logic of region assignment in focused and defocused images, average grayscale values of five random intracellular regions of three cells were plotted in scatterplots. As seen in Figure 2, the average grayscale values of only two regions (cell 1, threshold focused image) were above the threshold intensity (1800), whereas other regions showed intensities that were lower than the threshold. Hence, two regions were assigned after image thresholding. In the threshold defocused image, the average grayscale values were higher than the threshold intensity and a uniform, consolidated TID was assigned (threshold defocused scatterplot). It should also be noted that slight defocusing of the image did not interfere with the accuracy of loading regions selected on the basis of a defocused image over a tightly focused image. The same can be seen in Figure 1b (overlay image), wherein the blue area over each cell represented an automatically loaded region (based on defocused image) and thus a single region was assigned around each cell. Each cell was represented as an individual region, and this allowed measurement of several features via region tools. Figure 1, panel 4, illustrates the correlation between TID and the refractive index of the objects. We assumed that the uniform TID in a defocused image was due to the reduced phase contrast at defocal plane.

Quantitative Estimation of Cell Viability. The cellular response to a foreign drug is highly complex as it may trigger many time-dependent cellular events. Delays in processing large samples may lead to misinterpretation of time-dependent drug-

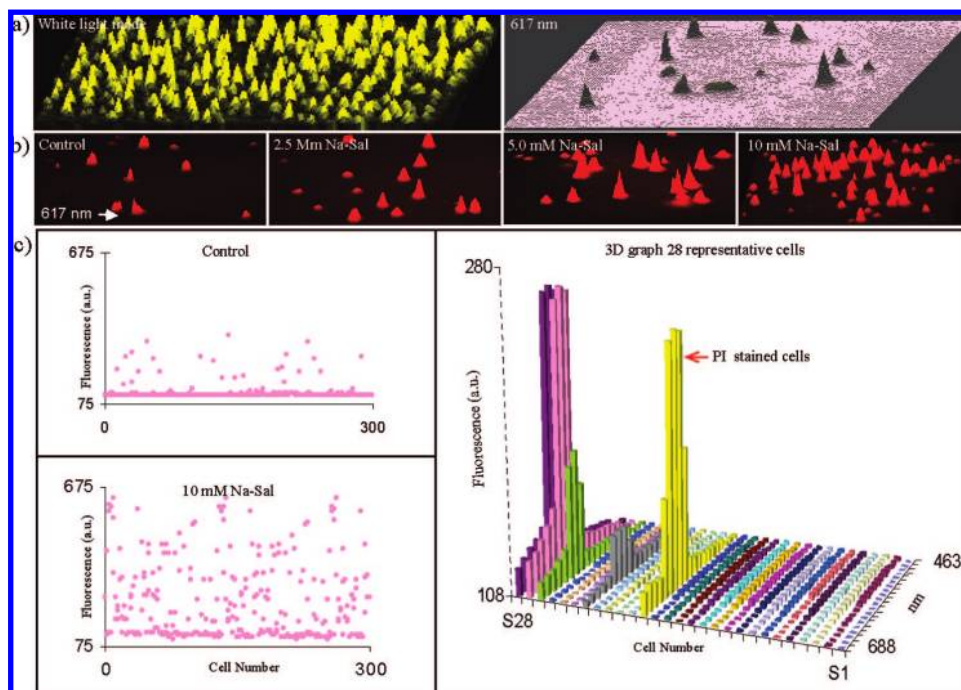


Figure 3. Methodology for quantitative cell viability measurement in HL-60 cells. (a) 3D cellular images of total cells based on their respective intensity profiles (under white light mode) and at 617 nm (emission maximum for PI). (b) Cellular images after 0 (control), 2.5, 5.0, and 10 mM Na-Sal treatment (12 h), respectively. Please refer to Table 1 for quantitative cell viability data. Scatter dot plots of 299 analyzed cells after 10 mM Na-Sal treatment (12 h) are shown in (c) based on their fluorescence intensities at 617 nm. (c) refers to the 3D graph of PI fluorescence intensities of 28 representative cells (i.e., from S1 to S28) plotted against AOTF filtering wavelengths.

Table 1. Quantitative Estimation of Cell Viability

drug	exposure time (h)	drug concn (mM)	percent cell viabilities (mean) in HL60 cells
naringenin	12	0	92
		0.10	77
		0.25	64
		0.50	43
		1.00	6
sodium salicylate	12	0	92
		2.50	83
		5.00	69
		10.00	45
camptothecin	6	0	92
		150 nM	68
		287 nM	57

induced cellular responses. Therefore, we focused on developing an automated and simple platform for rapid cell viability measurements. Cells were incubated in triplicate with various concentrations of CAM, NAR, and Na-Sal for different time intervals (2, 4, 6, 8, 12, and 24 h). HL-60 cells appeared to be sensitive to all three drugs under identical conditions. However, the extent of drug-induced cellular response, as determined by percent cell viability, was different for each drug. Figure 3 shows three-dimensional (3D) images of cells in white light mode and at the PI-positive wavelength, 617 nm. Table 1 illustrates the percent cell viabilities of the HL-60 cell line as a function of the three drugs and their concentrations. After 12 h of Na-Sal treatment, percent cell viabilities dropped from 83 to 45% as the drug concentration was increased from 2.5 to 10 mM. The same can be visualized in Figure 3, wherein images captured after 0 (control), 2.5, 5.0, and 10 mM Na-Sal (12 h) treatment can be seen. The number of PI-

stained cells increased gradually as the drug concentration increased. Scatter dot plots of 299 analyzed cells based on their fluorescence intensities at 617 nm are shown in Figure 3c. To better understand the developed methodology, 28 representative PI-stained and unstained cells are shown in a 3D graph as a function of AOTF filtering wavelength. A clear peak with maximum fluorescence intensity at 617 nm indicates PI-stained cells. As shown in Table 1, NAR treatment resulted in similar cell viabilities at a concentration almost 10 times less than that of Na-Sal. After 12-h exposure, there was a significant change in the percent viability of HL-60 cells (77 to 6%) as the concentration of drug was increased from 0.1 to 1 mM. Interestingly, CAM appeared to be effective even at a concentration 6 orders of magnitude lower than that of the other two drugs. After 6 h of incubation, cell viability was calculated to be 68 and 57% at drug concentrations of 150 and 287 nM, respectively. The standard deviation from three different measurements at the same concentration was less than 5%. The calculated standard error of estimation was as low as 0.025. These results were further verified by and in good agreement with the percent cell viabilities determined by conventional hemocytometric measurements. Figure 4 depicts a spider chart wherein the intracellular variation in the grayscale values of HL-60 cells after trypan blue treatment can be seen. The micrograph (white light mode) depicts the cellular morphology after trypan blue treatment. Grayscale values were taken randomly from three different regions (R1, R2, R3) of an individual HL-60 cell after trypan blue treatment. The result showed that the grayscale value of trypan blue-stained cell was lower than that of the partially stained or unstained cell. At the same time, differences in the grayscale values of trypan blue-stained, partially stained, and unstained cells were not sufficient

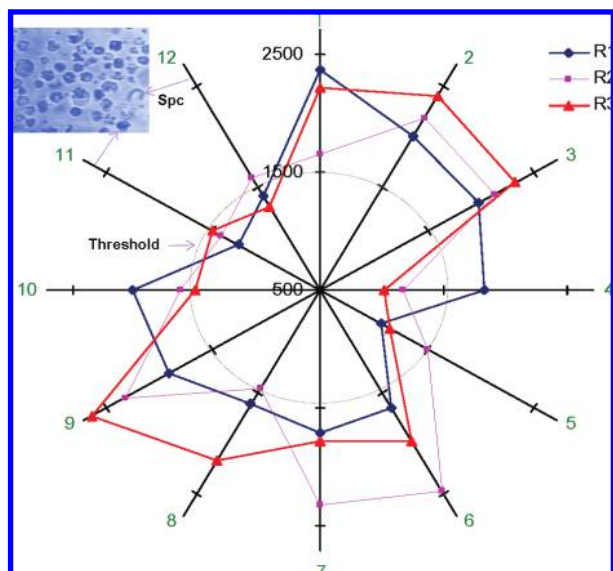


Figure 4. Spider chart illustrating the intracellular variation in the grayscale values (obtained by MetaMorph software) of HL-60 cells after trypan blue (0.25% in PBS) treatment. Spider chart displays 12 axes arms, i.e., lines labeled from 1 to 12. Each line (except line 12) represents an individual HL-60 cell after trypan blue treatment. Connecting lines in between the arms represents the grayscale values obtained from three different randomly chosen regions (R1, R2, R3) of an individual HL-60 cell. Line 12 refers to grayscale values obtained from three different randomly chosen regions of a serum protein coagulant (Spc). Micrograph (upper left) depicts morphological variations in the analyzed HL-60 cells.

enough to draw a distinct threshold parameter to distinguish viable and nonviable cells. Finally, the threshold value was adjusted to 1500, i.e., ~61% of the maximum grayscale value. Any cell with an average grayscale value below threshold value was considered nonviable, whereas the cell with an average grayscale value above the threshold value was considered as viable. The standard deviation obtained from three different readings under similar staining conditions was less than 16% of the average grayscale value.

Apoptosis and Necrosis Measurements. Figures 5 and 6 represent cellular images labeled with Qdot and PI taken under identical optical and staining conditions as described above. Confocal micrographs were taken along the AOTF filtering wavelengths. The optical spectrum represents increasing wavelength as a function of color (blue to red). Both CAM and NAR triggered the apoptosis cascade in HL-60 cells. Interestingly, apoptotic cells were observed to coexist with necrotic cells. In this regard, QMI cytometry offered efficient, simultaneous, and rapid discrimination of cell death pathways, which is otherwise difficult to visualize due to fast deterioration of early apoptotic cells to secondary necrosis. Considering the potential aggregation issues with Qdots, the captured images also showed successful labeling with Qdots and uniform distribution on the cell membrane (apoptotic cells). Hyperspectral fluorescence images of HL-60 cells after 6 h of CAM treatment are shown in Figure 5a (150 nM CAM) and Figure 6a (287 nM CAM). Compared to 150 nM CAM, 287 nM CAM induced rapid apoptosis in HL-60 cells. As indicated in Figure 5a, Apo 1, Apo 2, and Apo 3 cells exhibited a bright fluorescent ring around the cell membrane with maximum intensity at 523 nm. Thus, it can be inferred that PS moieties on

the apoptotic cell membrane were selectively stained by Annexin-Qdot, resulting in the fluorescent ring formation at the Qdot emission maximum (523 nm). PI 1, PI 2, and PI 3 cells showed maximum fluorescence intensity at 617 nm, which is the maximum emission wavelength of propidium iodide, indicating selective PI staining in these cells. The morphological changes during apoptosis helped to distinguish apoptosis from necrosis. The superimposed image, Figure 6a (lower right), shows fluorescence images taken at the 523 and 617 nm AOTF-filtering wavelengths and with irradiation of a halogen beam (white light) onto the cells. In Figure 6a, early apoptotic cells with PS externalization, membrane blebbing, and chromatin condensation can be observed. These cells, being early apoptotic, were highly selective for Annexin-Qdot and thus were not seen at PI-filtering wavelengths (617 nm). Figure 6b shows hyperspectral fluorescent images of HL-60 cells after 12 h of NAR (0.5 mM) treatment. The cell stained with both PI and Annexin-Qdot remained visible over the entire emission wavelength range (523–617 nm), indicating an early necrotic or late apoptotic phase of cell death. Along with staining for PS externalization, the cell was also stained with PI in cellular regions (see superimposed image), indicative of its gradual progression toward necrosis.

To better analyze the imaging data, the average fluorescence intensities of stained cells were obtained by Meta Imaging software. The 3D graph in Figure 5b represents the normalized average fluorescence intensities of apoptotic and necrotic cells taken over a range of filtering wavelengths (463–688 nm) at different time intervals. With wavelength-based separation along the y-axis and time-based separation along the x-axis graphed against the average fluorescence values, an interesting comparison among the acquired images is depicted. The normalized data revealed a clear discrimination between apoptotic and necrotic cells. The average signal intensities for Apo 1, Apo 2, and Apo 3 cells were maximal at 523 nm, whereas, for PI 1, PI 2, and PI 3 cells, the fluorescence intensities were maximal at 617 nm, similar to the known emission spectra of commercially available Qdot and PI. These data coincide with the results obtained through QMI cytometry.

As discussed earlier, the drugs used in our study have potent anticancer activity. CAM is reported to trigger an apoptotic cascade in cancer cell lines by selective interaction with type IB DNA topoisomerase enzyme.¹⁷ Na-Sal, a nonsteroidal anti-inflammatory agent (NSAIA), is known for its potent analgesic, antipyretic, and anti-inflammatory activity. It induces apoptosis in HL-60 cells through caspase-8 activation¹⁸ and mitogen-activated protein kinase signaling pathways.¹⁹ Similarly, NAR also has antioxidative and antiproliferative effects,²⁰ triggers apoptosis in HL-60 cells, and inhibits CYP3A4 activity.²¹ Therefore, to elucidate the fate of the aforementioned drug treatment on HL-60 cells, QMI cytometry was carried out and the results were compared with the earlier flow cytometric data.

- (17) Shellhaas, J. L.; Zuckerman, S. H. *Clin. Diagn. Lab. Immunol.* **1995**, 598–603.
- (18) Gac, S. L.; Vermes, I.; van den Berg, A. *Nano Lett.* **2006**, 6 (9), 1863–1869.
- (19) Portera-Cailliau, C.; Price, D. L.; Martin, L. J. *J. Comp. Neurol.* **1997**, 378, 70–87.
- (20) Matter, A. *Immunology* **1979**, 36, 179–190.
- (21) Shellhaas, J. L.; Zuckerman, S. H. *Clin. Diagn. Lab. Immunol.* **1995**, 2, 598–603.

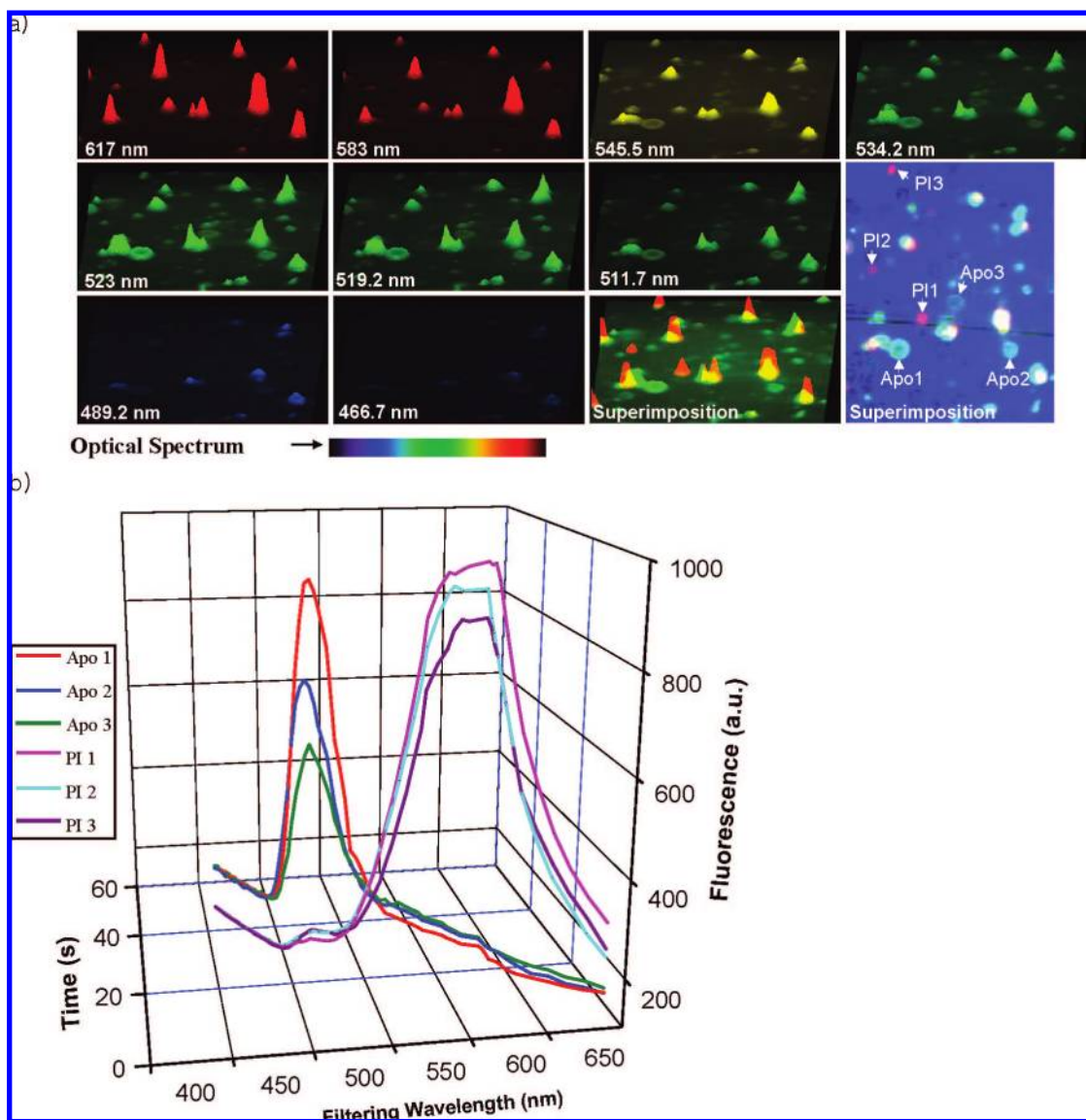


Figure 5. (a) Hyperspectral fluorescent images of HL-60 cells after 6 h of 150 nM CAM treatment. The images are taken over a spectral range from 463 to 688 nm with a total time interval of 60 s. Superimposed image in the lower right panel refers to the image under 523 nm, 617 nm, and visible wavelength (white light). (b) Apo 1, Apo 2, and Apo 3 represent apoptotic cells, whereas PI 1, PI 2, and PI 3 represent necrotic cells. Peak fluorescence activities can be seen at 523 (apoptotic cells) and 617 nm (necrotic cells). Please refer to (a) for real-time images of the above cells.

Quantitative Estimation of Drug-Induced Apoptosis. The quantitative results obtained via QMI cytometry (Table 2) are in good accordance with commercial flow cytometric analysis. All the drugs tested were able to induce apoptosis in HL-60 cells. As shown in Figure 7a, the trends in percent apoptosis obtained by QMI cytometry and flow cytometry were similar. However, the magnitude of apoptosis differed with respect to each drug/drug concentration. CAM (287 nM) induced rapid apoptosis compared to 150 nM CAM. NAR (0.5 mM) was an optimal concentration for apoptosis induction after 12 h of incubation. For Na-Sal, 5 mM was the optimal dose to trigger the apoptotic cascade in HL-60 cells after 24-h incubation. In this case, the data were also validated with flow cytometric forward scatter analysis and were in good accordance with the obtained results. These results suggest that the QMI cytometer can perform functions similar to those of the commercially available flow cytometer and also provide the additional imaging data. For better understanding of the quantita-

tive data, scatter dot plots of a few representative samples (i.e., control (12 h), 287 nM CAM (4 h), 0.5 mM NAR (12 h), and 1 mM NAR (12 h)) are displayed in Figure 7b. In it, the lower right quadrant shows early apoptotic cells (Annexin V–Qdot positive) and the upper left quadrant shows PI positive (necrotic) cells.

DISCUSSION

Over the past few decades, automation in cellular assays has been synonymous with handling larger samples in smaller assay volumes with sensitive and quantitative detection schemes. In this context, image-based cellular assays appear to combine assorted problems with regard to quantitative analysis. Quantitative analysis based on a standard curve needs timely optimization of quantitative standards (standard curve) due to the deterioration of the chemical stocks and buffers used for cellular assays. Here we have presented a versatile, automated, quantitative, and multivariate

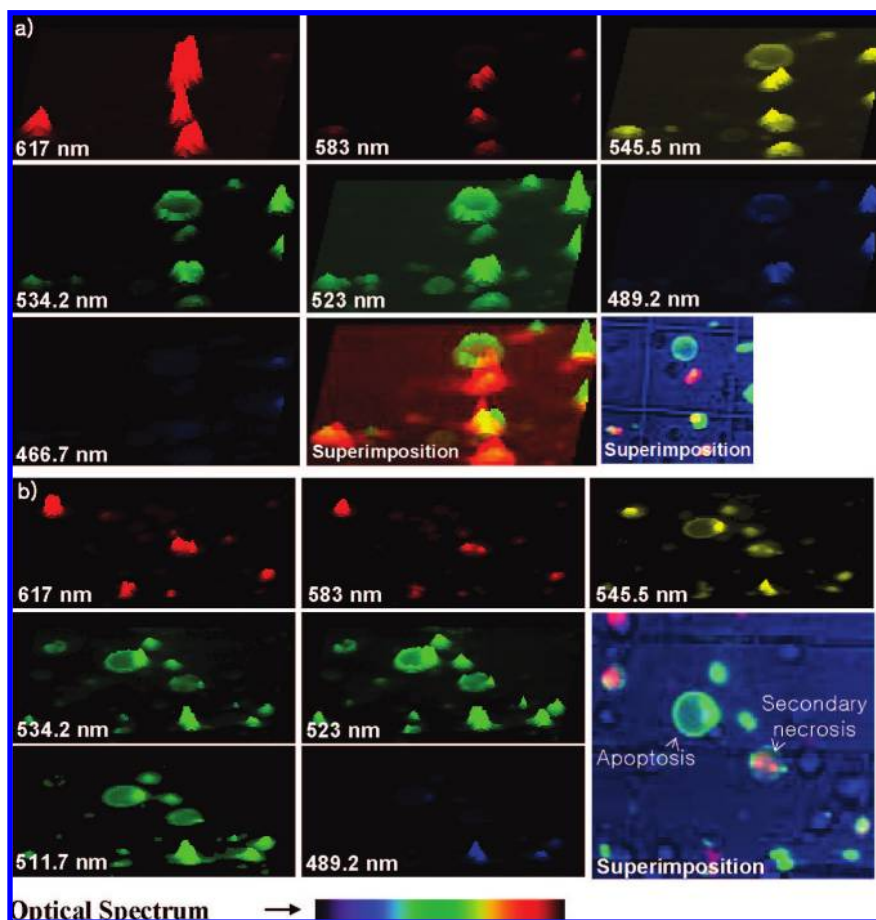


Figure 6. Hyperspectral fluorescence images of HL-60 cells. (a) After 6 h of 287 nM CAM treatment. (b) NAR (0.5 mM) treatment for 12 h. Superimposed image in the lower right panel refers to images taken together under 523 nm and at visible wavelength (white light).

Table 2. Quantitative Estimation of Apoptosis by QMI Cytometry

sample ID	samples	quadrant			
		UL ^a	UR ^b	LL ^c	LR ^d
1	CAM ^e control (12 h)	2.00	4.00	89.00	5.00
2	CAM 150 nM (4 h)	2.00	12.00	67.00	19.00
3	CAM 150 nM (8 h)	5.00	8.00	55.00	32.00
4	CAM 150 nM (12 h)	3.00	65.00	23.00	9.00
5	CAM 287 nM (2 h)	4.00	14.00	77.00	5.00
6	CAM 287 nM (4 h)	1.00	17.00	45.00	37.00
7	CAM 287 nM (6 h)	2.00	52.00	32.00	14.00
8	NAR ^f control (12 h)	1.00	0.00	94.00	5.00
9	NAR 0.1 mM (12 h)	2.00	15.00	58.00	25.00
10	NAR 0.25 mM (12 h)	1.00	8.00	59.00	32.00
11	NAR 0.5 mM (12 h)	3.00	22.00	36.00	39.00
12	NAR 1 mM (12 h)	8.00	45.00	29.00	18.00
13	Na-Sal ^g Control (24 h)	0.00	6.00	89.00	5.00
14	Na-Sal 2.5 mM (12 h)	1.00	11.00	78.00	10.00
15	Na-Sal 5 mM (12 h)	3.00	16.00	69.00	16.00
16	Na-Sal 5 mM I (24 h)	2.00	17.00	51.00	30.00

^a Upper left. ^b Upper right. ^c Lower left. ^d Lower right. ^e Camptothecin. ^f Naringenin. ^g Sodium salicylate. UR quadrant indicates percent secondary necrosis; LR quadrant indicates percent apoptosis.

protocol for image-based cellular assays that does not require a standard curve.

Toxicity is a major cause of drug failure during drug development. Therefore, the drug discovery process aims to improve drug efficacy and selectivity for cancer-specific targets with minimal

toxicity. Regarding CAM- and NAR-induced cytotoxicity, an earlier report indicates that the switch in fate from apoptosis to necrosis is unknown.²² Results obtained via QMI cytometry were quite promising in elucidating the fate of these drugs against cancer cells. Quantitative apoptosis and cell viability measurements obtained by QMI cytometry with further validation through flow cytometric and manual hemocytometric measurements revealed drug-induced cellular responses at various drug concentrations.

The results presented herein clearly demonstrate the reliability of QMI cytometry compared to automated, trypan blue-based cell viability measurements. This difference in reliability is caused by the reduction in the grayscale values after trypan blue staining, which is not enough to draw a clear distinction (threshold) between stained, partially stained, and unstained cells. Hence, in many events, the grayscale values for an individual cell lie on both sides of the threshold value, calling into question the reliability of the trypan blue assay method. It should be noted that the reduction in grayscale values can also occur due to the absorption of white light by unevenly distributed cellular moieties and culture contaminants, irrespective of trypan blue dye. In addition, culture contaminants can also absorb vital dye (see line 12, a serum protein coagulant (Spc) in Figure 4) and hence can produce misleading results. These facts make the assay more ambiguous and often result in less statistical confidence, as shown in our

(22) Akerman, M. E.; Chan, W. C.; Laakkonen, P.; Bhatia, S. N.; Ruoslahti, E. *Proc. Natl. Acad. Sci. U. S. A.* **2002**, *99*, 12617.

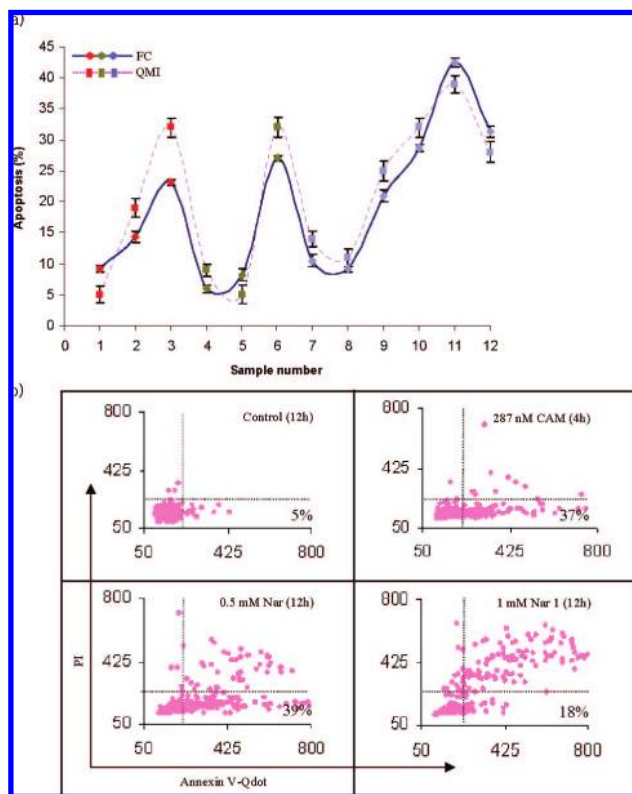


Figure 7. (a) Validation of drug-induced apoptosis in HL-60 cells by comparing the results obtained with QMI cytometry with those from flow cytometry (FC). X-axis represents different drugs/drug concentrations (see Table 2 wherein sample IDs 1–12 refer to the x-axis values (sample numbers 1–12), respectively). Y-axis represents percent apoptosis. (b) Scatter dot plots obtained via QMI cytometry displaying the quantitative apoptosis measurements in the HL-60 cell line after 287 nM CAM (4 h), 0.5 mM NAR (12 h), and 1 mM NAR (12 h) treatment with respect to control (12 h). Lower right (LR) quadrant represents percent apoptosis.

results (Figure 4). In contrast, the difference in the fluorescence values of PI-stained and unstained cells in QMI-based cell viability measurements were sufficient to fix threshold values to discriminate viable and nonviable cells, i.e., ~3-fold more than the difference in the grayscale values of trypan blue-stained and unstained cells.

Cell death and the subsequent postmortem changes (necrosis) are a constitutional part of normal development and the cell maturation cycle. In cancer treatment, the preferred approach is the removal of neoplasm by surgery or by killing neoplastic cells with radiation, anticancer drugs, antibodies, and immune cells. Thus, understanding the mode of cell death has gained special importance in finding lead selections during anticancer drug screening. However, the physiological and biochemical factors that lead to cell death remain poorly understood because the physiological and biochemical events are highly complex, share similar intermediates, and often last for only a few seconds. This leads to overlapping of the antemortem and postmortem cellular events and subsequent interference in diagnostic methodology. Thus, it is difficult to discriminate the cell death fate even when using the latest diagnostic tools. The inherent qualities of QMI cytometry, such as rapid, automated, and selective wavelength scanning, have allowed clear-cut distinction between the modes of cell death (apoptosis and necrosis), both experimentally and mechanistically.

Rapid imaging based on rapid wavelength tuning through QMI has allowed clear discrimination between apoptotic and necrotic cells (Figure 5) by eliminating the incorporation of vital dye (PI) into the early apoptotic cells. Similarly, QMI also offers simultaneous monitoring of the hybrid form of cell death (between apoptosis and necrosis, Figure 6b). The additional depiction of cellular morphology has added an extra dimension with which the fate of cell death can be predicted and tallied with simultaneous spectral analysis for better stability of the developed protocol. With regard to quantitative apoptotic analysis, similarities in the percent apoptosis obtained with QMI cytometry and with flow cytometry suggest that the developed protocol can complement certain flow cytometric assays.

In recent years, several imaging modalities and systems have been established for quantitative cell-based assays. Most of these systems facilitate either homogeneous or intact cellular assays, e.g., cell viability, caspase activation, etc., based on a specific indicator dye or an enzyme–substrate. These systems can not provide both cellular counting and high content screening simultaneously. This is due to the interference of an indicator dye (used for cellular staining) to the fluorescent-tagged intracellular biomolecules. Another rapid approach can be bright-field imaging microscopy wherein TID-based cellular counting can be achieved without cellular staining. To date, quantitative cellular measurements using bright-field microscopy are a challenge due to uneven TID in a tightly focused cellular image. In this regard, the developed approach, i.e., uniform TID-based QMI cytometry, has provided successful quantitative cellular measurements in the bright-field cellular imaging along with the simultaneous monitoring of intracellular biomolecules. Considering the amenability to biofunctionalization, unique photostability, narrow emission, and broad excitation spectra of Qdots,²³ multicolor imaging revealed an efficient discrimination of Annexin–Qdot and PI-stained cells by QMI cytometry with higher spectral resolution between the fluorophores. This result suggests that Qdots can be used as an efficient probe in multispectral and multicolor imaging analysis. To avoid further complications associated with Qdot toxicity,²⁴ and its intracellular permeability in live cell imaging, we have used biofunctionalized Qdots to label PS moieties present on the outer side of the cellular membrane. As far as potential aggregation issues of Qdots in cellular imaging are concerned, we successfully labeled cells with Annexin–Qdots with its uniform distribution on cellular PS moieties. Acquired fluorescent images within the spectral range (463–688 nm) showed rapid, clear discrimination of early apoptotic, late apoptotic, and necrotic cellular events with photostable detection and high spectral resolution. These features offer great promise in elucidating the drug-induced cell death pathways with special reference to anticancer drugs. The lower standard deviation obtained in cellular assays may be attributed to the use of rapid imaging, selectable wavelength tuning through QMI cytometry, and a direct analytical approach for quantitation without the use of a standard curve.

As described earlier, image-based quantitative analysis is associated with several practical difficulties during the assay procedure. The most typical and unresolved difficulty is the intracellular variation in *z* values due to uneven TID during

(23) Gac, S. L.; Vermes, I.; van den Berg, A. *Nano Lett.* **2006**, *6* (9), 1863–1869.

(24) Singh, S.; Nalwa, H. S. *J. Nanosci. Nanotechnol.* **2007**, *7* (9), 3048–70.

threshold adjustment of an image. Thus, it is quite difficult to select each cell as an individual region based on its grayscale values. Initially, we have tried to blur or filter the image to achieve uniform TID over the objects. Blurring or filtering the image resulted in minimizing the overall differences in the grayscale values over the object, but at the same time, software failed to assign an individual region around each cell. On the other hand, slight defocusing of an image proved to be the best remedy for this problem. With this approach, cells with different z values appeared similar when the micrograph was taken slightly away from the focal point of the image, allowing uniform TID over the background-nullified image (See Figure 2 for details.). Uniform and consolidated TID is an important parameter in assigning an individual region around a cell. Once a cell has been assigned an individual region, many cellular parameters can be automatically identified along with the quantitative measurements. Uniform threshold intensity distribution in the obtained defocused images clearly indicates the importance of defocusing in achieving highly quantitative measurements by achieving a uniform and consolidated TID.

Commercially available softwares for quantitative analysis use TID as a parameter to assign an individual region to an individual object present on the sample image. In order to achieve high accuracy in cellular counting, each cell should be assigned as an individual object. Uneven TID may result in the assignment of two or more regions to an individual cell, leading to misinterpretation in the quantification of the total number of cells present on a cellular image. The obtained results proved that the intracellular TID in the tightly focused image was not uniform, and hence, the software failed to create an individual region around each cell. On the contrary, almost all the cells were assigned with an individual region when the same image was slightly defocused. This is mainly based on the fact that phase contrast is reduced at the defocused plane compared to at the focal plane. As objects recede from the focal plane, the phase contrast due to difference of refractive indexes of objects becomes less obvious, and as a result, more uniform TID of objects can be accomplished. This can be well explained by relative refractive index theory, wherein highly refractive molecules such as cellular granules bend light to a much greater angle than vacuoles having low refractive index. As a result, cellular granules appear much darker than vacuoles. Here, refractive index $n = C/v_p$ refers to the ratio of light velocity (C) in air to the light velocity in side the cellular environment (v_p). The obtained results revealed that the objects on a defocused image had similar grayscale values representing uniform TID due to reduced phase contrast of objects at that particular defocal plane, whereas the uneven distribution of grayscale values in the tightly focused image might arise from high phase contrast of objects at the focal plane, leading to an ununiform TID (Figure 1; panel 4).

This work demonstrates that the protocol based on QMI cytometry combined with fluorescent semiconductor nanocrystals can be used for various cellular assays and as a generalized platform for quantitative cellular image-based analysis. This is a versatile protocol and can be adapted to various cell types. With this approach, the present manual hemocytometric analysis for cell viability measurements can be completely automated. The current automated, quantitative cell viability measurements based

on a vital trypan blue dye has several limitations as the average grayscale intensities are taken in white light mode and not at a specific wavelength range. This can produce misleading results due to cross-reactivity of the vital dye (broad emission spectra) with various other contaminants, resulting in low statistical confidence during the assay procedure. Quantitative multicolor and multispectral apoptotic analysis, with further comparison to flow cytometry, suggested that the developed protocol can surpass flow cytometry in certain aspects due to its ability to provide additional imaging data. Furthermore, the developed assay can overcome the difficulties inherent in flow cytometric assays. For example, problems associated with stickiness and trypsinization of adherent cells can be best resolved using QMI cytometer. It is more miniaturized, less costly, and easier to operate than the flow cytometer. A commercial flow cytometer has ~ 8 detectors; hence, the multicolor/multispectrum analysis is limited to 8 target molecules. On the other hand, the QMI cytometer provides a wide range of filtering (scanning) wavelengths at ~ 3.75 -nm intervals, making the system more compatible for high-throughput screening. Moreover, QMI cytometry allows live-cell monitoring to visualize drug-induced cellular responses, which is not possible with flow cytometry. With selective wavelength tuning, QMI cytometry can also minimize the problems associated with unwanted autofluorescence of cells during cellular imaging analysis. Thus, the developed protocol allows rapid, quantitative, and automated analysis to visualize and quantify targeted cellular moieties, while simultaneously exemplifying the possible mechanism involved in drug-induced cellular pathways, i.e., cascade of simultaneous cellular events. Since the developed approach is the first of its kind, we have intentionally chosen already established assays, for example, apoptosis/necrosis and cell viability for quantitative measurements. The validation of obtained results with flow cytometry suggests that QMI cytometry can be used for simultaneous monitoring of various intracellular biomolecules by rapid multicolor/multispectral analysis, which in fact can not be achieved by filter-based conventional imaging systems. Thus, our future research is based on the elucidation of cellular cascades by simultaneous monitoring of various targeted intracellular moieties using QMI cytometry. Using marketed drugs as examples, the present study also suggests a system for profiling the in vitro properties of anticancer drugs. Owing to the compatibility, the simplicity, and the ability to monitor alterations in an individual cell over time, the developed protocol may complement certain flow cytometric assays. Further exploration of these concepts may have fundamental significance in establishing image-based assays for targeted biomolecules through the use of this developed protocol.

CONCLUSION

We report a tool for an automatic, rapid, quantitative cellular imaging analysis based on uniform threshold intensity distribution. We believe that the developed method will add new dimensions in implementing quantitative analytical approaches to image-based cellular assays. This will also contribute in performing a wide type of arrays for multivariate cellular assays via single-cell monitoring over time. In context to high-throughput drug screening

technology, QMI cytometry can pave a way for new generation anticancer drug screening by complementing certain flow cytometric measurements.

ACKNOWLEDGMENT

This work was supported by the Korea Science and Engineering Foundation (KOSEF) grant funded by the Korean Ministry of Science and Technology (MOST) under contract

M1064408000306N440800310 along with M1074004000207-N400400211 program with Seoul National University.

Received for review March 4, 2008. Accepted May 1, 2008.

AC800452X